

Post-Perihelion Integral Field Spectroscopy of the Interstellar Comet 3I/ATLAS

WILLEM B. HOOGENDAM,^{1,*} DAVID O. JONES,² BIN YANG,^{3,4} BENJAMIN J. SHAPPEE,¹ JAMES J. WRAY,^{5,1} KAREN J. MEECH,¹ CHRISTOPHER ASHALL,¹ DHVANIL D. DESAI,¹ JASON T. HINKLE,^{6,7,1,†} ANDREW M. HOFFMAN,¹ KYLE MEDLER,¹ CAMERON PFEFFER,¹ AND RUINING ZHAO⁸

¹*Institute for Astronomy, University of Hawai‘i, 2680 Woodlawn Drive, Honolulu, HI 96822, USA*

²*Institute for Astronomy, University of Hawai‘i, 640 N. A‘ohoku Pl., Hilo, HI 96720, USA*

³*Instituto de Estudios Astrofísicos, Facultad de Ingeniería y Ciencias, Universidad Diego Portales, Santiago, Chile*

⁴*Planetary Science Institute, 1700 E Fort Lowell Rd STE 106, Tucson, AZ 85719, USA*

⁵*School of Earth and Atmospheric Sciences, Georgia Institute of Technology, 311 Ferst Drive, Atlanta, GA 30332, USA*

⁶*Department of Astronomy, University of Illinois Urbana-Champaign, 1002 West Green Street, Urbana, IL 61801, USA*

⁷*NSF-Simons AI Institute for the Sky (SkAI), 172 E. Chestnut St., Chicago, IL 60611, USA*

⁸*National Astronomical Observatories, Chinese Academy of Sciences, Beijing 100101, China*

ABSTRACT

The environs of other stellar systems may be directly probed by analyzing the cometary activity of interstellar objects. The recently discovered interstellar object 3I/ATLAS was the subject of an intensive worldwide follow-up campaign in its pre-perihelion approach. Now, 3I/ATLAS has begun its post-perihelion departure from the Solar System. In this letter, we report the first post-perihelion blue-sensitive integral-field unit spectroscopy of 3I/ATLAS using the Keck Cosmic Web Imager on November 16, 2025. We confirm previously reported CN, Fe, and Ni outgassing along with detections of carbon chain molecules C₂ and C₃. We calculate production rates for each species. We find Fe and Ni production rates of $Q_{\text{Fe}} = (9.55 \pm 3.96) \times 10^{25}$ atoms s⁻¹, and $Q_{\text{Ni}} = (6.61 \pm 2.74) \times 10^{25}$ atoms s⁻¹, resulting in a ratio of $\log(Q_{\text{Ni}}/Q_{\text{Fe}}) = -0.16 \pm 0.03$, which matches Solar System comets well and continues the pre-perihelion trend of declining $\log(Q_{\text{Ni}}/Q_{\text{Fe}})$ with r_h . We investigate the radial distributions of these elemental species and find characteristic *e*-folding radii of 3880 ± 39 km for Ni, 6053 ± 68 km for CN, 4194 ± 45 km for C₂, and 3833 ± 45 km for C₃. Compared to pre-perihelion measurements, these radii have increased by a factor of $\sim 6.5\text{--}7$. Our post-perihelion observations reveal that 3I/ATLAS continues to exhibit cometary behavior broadly consistent with Solar System comets.

Keywords: Asteroids (72); Comets (280); Meteors (1041); Interstellar Objects (52); Comet Nuclei (2160); Comet Volatiles (2162); Small Solar System Bodies (1469); Astrochemistry (75); Planetesimals (1259)

1. INTRODUCTION

Comets and asteroids ejected from other stellar systems are predicted to intercept the solar system by chance at a frequent rate (e.g., Engelhardt et al. 2017), yet the discovery of these objects has been limited to three exceptional examples: 1I/‘Oumuamua (Meech et al. 2017; ‘Oumuamua ISSI Team et al. 2019), 2I/Borisov (Borisov et al. 2019; Jewitt & Luu 2019; Guzik et al. 2020), and now, 3I/ATLAS (Denneau et al. 2025; Seligman et al. 2025; Tonry et al. 2025), which was

recently discovered by the Asteroid Terrestrial-impact Last Alert System (ATLAS; Tonry et al. 2018, 2025). Just as small bodies in our Solar System reflect its primordial composition (e.g., Bodevits et al. 2024), interstellar objects are likewise probes of the composition and evolution of small bodies around different stars (e.g., Jewitt & Seligman 2023; Fitzsimmons et al. 2024).

To date, each interstellar object has shown unique activity signatures. Despite observations throughout its brief window of visibility, a coma or outgassing activity was undetected for 1I/‘Oumuamua (e.g., Meech et al. 2017; Ye et al. 2017; Jewitt et al. 2017; ‘Oumuamua ISSI Team et al. 2019; Trilling et al. 2018); however, outgassing was inferred from its non-gravitational accel-

* NSF Graduate Research Fellow

† NHFP Einstein Fellow

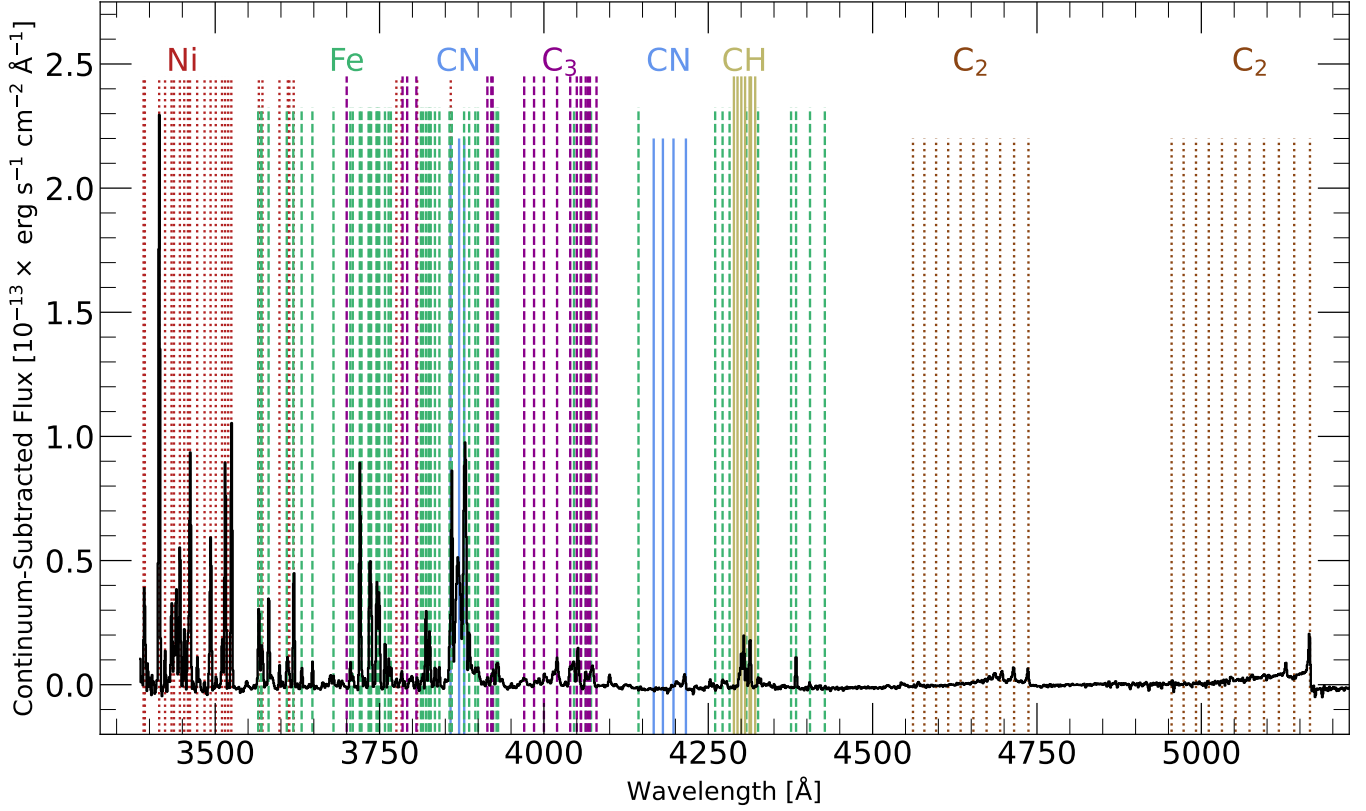


Figure 1. The continuum-subtracted KCWI spectrum of 3I/ATLAS between 3325 Å and 5225 Å, extracted from a 2'' aperture centered on the comet. Cometary emission species are denoted as follows: Ni as red dotted lines, Fe as green dashed lines, CN as solid blue lines, C₂ as dotted light purple lines, and C₃ as dashed dark purple lines. The C₂ and C₃ lines shown may not be individually resolved.

eration (Micheli et al. 2018). Contrarily, 2I/Borisov was clearly outgassing, had a dusty coma (Fitzsimmons et al. 2019; Jewitt & Luu 2019; Cremonese et al. 2020; Guzik et al. 2020; Hui et al. 2020; Kim et al. 2020; McKay et al. 2020; Ye et al. 2020; Yang et al. 2021), and displayed many features commonly observed in Solar System comets (e.g., Opitom et al. 2019; Fitzsimmons et al. 2019; Lin et al. 2020; McKay et al. 2020; Xing et al. 2020; Bannister et al. 2020), including Ni and Fe outgassing (Guzik & Drahus 2021; Opitom et al. 2021).

3I/ATLAS is likewise undergoing cometary activity and has a visible coma (Seligman et al. 2025; Jewitt et al. 2025; Cordiner et al. 2025; Rahatgaonkar et al. 2025; Opitom et al. 2025; de la Fuente Marcos et al. 2025; Chandler et al. 2025; Lisse et al. 2025; Hoogendam et al. 2025a; Tonry et al. 2025). The initial spectra exhibited red-sloped reflectance without strong emission features (Seligman et al. 2025; Opitom et al. 2025; Puzia et al. 2025). As it approached perihelion, outgassing increased. Absorption from large water ice grains in the coma (Yang et al. 2025) and emission from CN (Rahatgaonkar et al. 2025), Ni (Rahatgaonkar et al. 2025), CO₂ (Lisse et al. 2025; Cordiner et al. 2025), CO (Cordiner

et al. 2025), and a likely extended source of OH emission (Xing et al. 2025) has been reported.

Integral field unit (IFU) data provide several advantages over slit spectroscopy, including the addition of spatial information. Previous blue-sensitive IFU data for 3I/ATLAS include those presented by Seligman et al. (2025) and Hoogendam et al. (2025b) from the Super-Nova Integral Field Spectrograph (SNIFS; Lantz et al. 2004, see also Tucker et al. 2022) and Keck Cosmic Web Imager (KCWI; Morrissey et al. 2018) presented by Hoogendam et al. (2025a). The latter revealed centrally concentrated Ni emission relative to CN with a less extended radial distribution. Here, we present the first post-perihelion IFU observations of 3I/ATLAS from KCWI.

2. DATA

We obtained a KCWI spectrum of 3I/ATLAS on UTC 2025-Nov-16 14:44:08 (observation start), along with two solar analogs (HD 103218 and HD 103390) and a flux calibration standard (Feige 67) at a similar airmass (~ 3 , due to solar and lunar constraints). 3I/ATLAS was at heliocentric (r_h) and geocentric (Δ) distances of

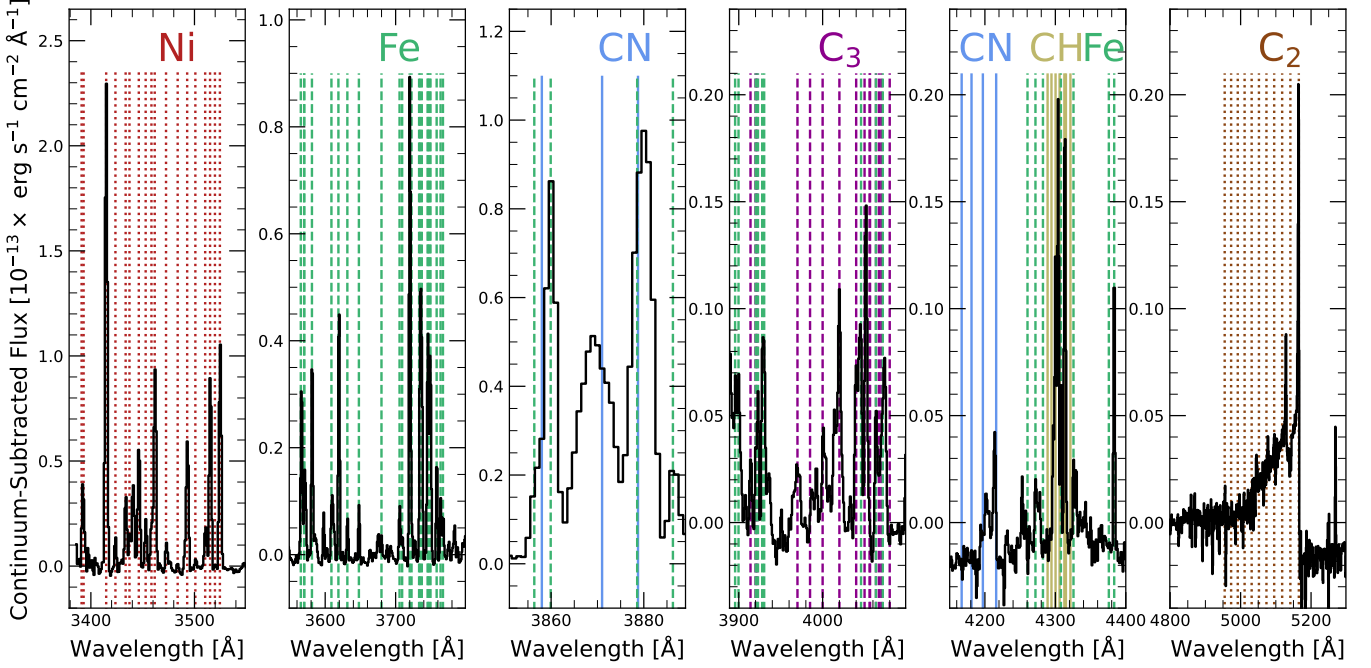


Figure 2. The same as Figure 1, but with individual panels for each emission feature.

1.509 au and 2.089 au, respectively, at the start of the observations. The phase angle was 26.049° , and the true anomaly was 28.099° .

Our KCWI configuration used the medium image slicer, which provides a $16.5''$ by $20.4''$ field of view with a slice width of $0.70''$. The blue/red channel used the BL/RL gratings, respectively. These provide a spectral resolving power of $R \approx 1800$ in the blue from ~ 3300 Å to ~ 5500 Å and $R \approx 1000$ in the red from ~ 5500 Å to ~ 9000 Å in the red. The total on-source integration time was 300 s for the blue channel and 420 s for the red channel. Because 3I/ATLAS filled the entire medium slicer field of view, we also took separate sky frames near 3I/ATLAS in an empty field to enable accurate sky subtraction. Finally, we used a $2''$ aperture to extract 1D spectra from the cubes.

We reduced the data using the KCWI Data Reduction Pipeline (DRP; Neill et al. 2023) but disabled the pipeline’s sky subtraction and flux calibration. Instead, we performed manual sky subtraction and flux calibration using the differential-atmospheric-refraction-corrected cubes. We extracted 1D spectra from the separate sky frames in the same manner as for the science observations, then median-combined them to produce a master sky spectrum, which was subtracted from the final target spectrum. We flux-calibrated the sky-subtracted frames using the CALSPEC reference spectrum of Feige 67 to compute a sensitivity function; the spectra were then multiplied by this function to produce flux-calibrated spectra. Lastly, we combined the spectra

using inverse-variance weighting to produce final spectra for 3I/ATLAS and the two solar analog stars.

3. SPECTROSPATIAL ANALYSIS OF 3I/ATLAS

To subtract the solar continuum contribution, we use HD 203218 as a solar analog. We model the continuum in the same manner as Rahatgaonkar et al. (2025) and Hoogendam et al. (2025a). This model has a functional form of

$$F_{\text{cont}}(\lambda) = R(\lambda) \times F_{\odot\text{analog}} \left[\lambda \left(1 + \frac{v}{c} \right) + \delta\lambda \right]. \quad (1)$$

In this model, the second-order polynomial $R(\lambda) \equiv \frac{1}{S} (1 + b_1\lambda + b_2\lambda^2)$ models the cometary reflectance as a function of the the b_1 and b_2 parameters. The reflectance function is normalized by a factor S to compensate for flux differences between the comet spectrum and the solar analog spectrum. Of note, 3I/ATLAS and the analog stars have a similar magnitude, making the normalization factor S near unity in this instance. $F_{\odot\text{analog}}$ is the solar analog flux, and is shifted by fitted nuisance parameters v and $\delta\lambda$.

Figure 1 shows the 3325 Å to 5225 Å 1D continuum-subtracted spectrum from our KCWI datacube, and Figure 2 shows the same continuum-subtracted spectrum over the wavelength ranges for each observed feature.

3.1. Activity Signatures

Optical spectroscopy of 3I/ATLAS initially revealed pre-perihelion emission of Ni and CN (Rahatgaonkar et al. 2025; Hoogendam et al. 2025a,b; Salazar Manzano

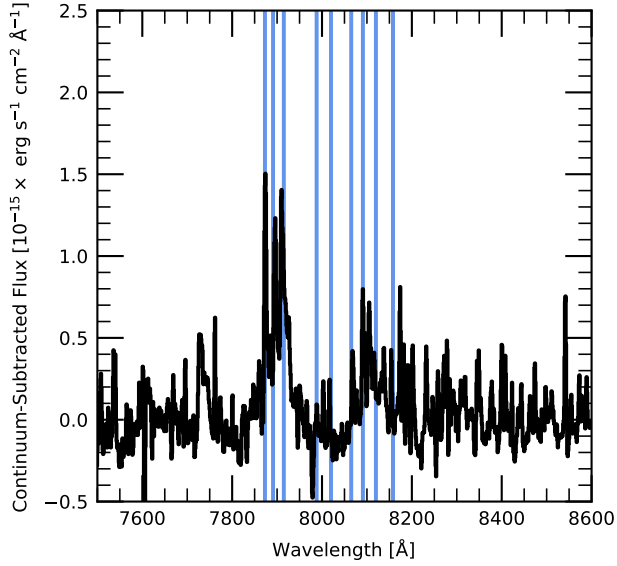


Figure 3. The continuum-subtracted KCWI spectrum of 3I/ATLAS between 7500 Å and 8600 Å, extracted from a 3'' aperture centered on the comet. The red CN system is shown in blue.

et al. 2025), followed by detections of Fe (Hutsemékers et al. 2025). Astronomer's Telegrams from Bolin et al. (2025a), Jehin et al. (2025a), and Jehin et al. (2025b) report pre-perihelion detections of C_2 and C_3 and Ganesh et al. (2025) and Bolin et al. (2025b) report the same in post-perihelion data.

We show post-perihelion detections of classic comet features such as C_2 ($d^3\Pi_g - a^3\Pi_u$ (0,0) and (1,0) lines; Swan 1857), C_3 ($A^1\Pi_u - X^1\Sigma_g^+$ lines; Huggins 1881; Gausset et al. 1965), and CH ($A^2\Delta - X^2\Pi$ (1,1) lines; Meier et al. 1998), and find continued Ni and Fe activity, even after solar passage. Additionally, while Hoogendam et al. (2025b) and Salazar Manzano et al. (2025) only report detecting the CN violet system ($B^2\Sigma^+ - X^2\Sigma^+$, $\Delta\nu = 0$) near 3870 Å, we detect two additional CN sequences: the CN blue system ($B^2\Sigma^+ - X^2\Sigma^+$, $\Delta\nu = +1$) near ~ 4200 Å and the CN red system ($A^2\Pi - X^2\Sigma^+$, $\Delta\nu = +1$) near ~ 8000 Å (Figure 3).

We use a simple Haser (1957) model to convert the measured line fluxes into gas production rates for CN, C_2 , and C_3 . The number of photons emitted per molecule per second (i.e., the g -factor) and the scale lengths were taken from A'Hearn et al. (1995). The extracted spectrum has a physical radius of ~ 3000 km. Our calculation assumes an isotropically escaping gas at a constant velocity originating from the nucleus. We adopt a mean expansion speed of $0.8 \times r_h^{-0.6}$ km s $^{-1}$, following Biver et al. (1999), where r_h is the heliocentric distance in au. The derived production rates

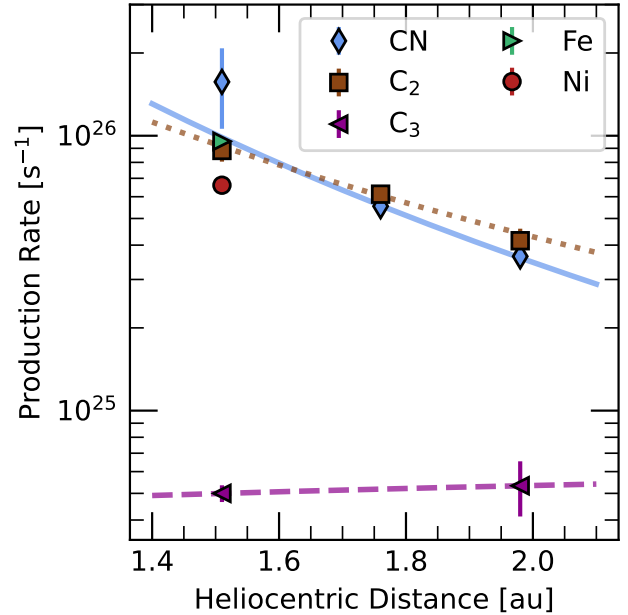


Figure 4. Post-perihelion production rate evolution as a function of heliocentric distance using data from this work at $r_h = 1.509$ au and rates reported from TRAPPIST measurements (Jehin et al. 2025a,b). CN and C_2 have similar exponential decays, whereas C_3 is nearly constant. Best-fit power laws are shown as the solid (CN), dotted (C_2), and dashed (C_3) lines.

are $Q_{CN} = (1.6 \pm 0.5) \times 10^{26}$ molecules s $^{-1}$, $Q_{C_2} = (8.8 \pm 0.8) \times 10^{25}$ molecules s $^{-1}$, and $Q_{C_3} = (5.0 \pm 0.4) \times 10^{24}$ molecules s $^{-1}$. The logarithmic ratio between Q_{C_2} and Q_{CN} is -0.26 ± 0.14 , and between Q_{C_3} and Q_{CN} is -1.51 ± 0.14 . Although still C-chain depleted, this ratio is higher than the pre-perihelion upper limit ($\log(Q_{C_2}/Q_{CN}) \leq -0.8$, Salazar Manzano et al. 2025).

Subsequent production rates from TRAPPIST observations at $r_h = 1.76$ au find the activity decreases as 3I/ATLAS moves farther away from the Sun ($Q_{CN} = (5.5 \pm 0.2) \times 10^{25}$ molecules s $^{-1}$; Jehin et al. 2011; Jehin et al. 2025a), and even later TRAPPIST measurements (Jehin et al. 2025b) find a $\sim 50\%$ decrease in production rate from $r_h = 1.76$ au to $r_h = 1.98$ au, a trend that is consistent with our measurements despite the difference in profile and Haser (1957) model assumptions.

We show the post-perihelion production rates reported to date in Figure 4. We also fit the post-perihelion production rate evolution with a simple power law defined as $C \times (r_h)^n$, where C is a constant and r_h is the heliocentric distance in au. CN and C_2 have similar power law indices, whereas C_3 is nearly constant. A positive or flat heliocentric distance slope is not seen in any of the 85 comets in A'Hearn et al. (1995), sug-

gesting this trend for C_3 in 3I/ATLAS may arise from a non-physical driver, such as different assumptions in the computation of production rate (although we note that if so, the CN and C_2 trends do not have this issue).

At larger heliocentric distances, CN production is commonly attributed to photolysis of HCN, although CN can also receive contributions from the degradation of complex refractory organic material on dust grains (A'Hearn et al. 1995; Fray et al. 2005). The steep decline in CN production is therefore consistent with dominance by a near-nucleus volatile source whose release decreases rapidly as insulation drops. The shallower heliocentric dependence observed for C_2 suggests a larger contribution from a distributed grain source. In contrast, the near-zero slope for C_3 may indicate that its production is dominated by a distributed source whose contribution is delayed post-perihelion. However, if such a distributed source violates the assumptions of the Hauer model, the derived production rates may acquire a spurious heliocentric dependence (Cochran 1985).

We interpret the Fe I and Ni I emission lines using a simplified three-level atom approximation consisting of the ground state, a metastable lower level, and an excited upper level populated by resonance fluorescence under diluted solar radiation (Preston 1967; Arpigny et al. 1978). Under statistical equilibrium and negligible collisional effects, the line intensities follow a Boltzmann-type relation: $\log_{10}(I \lambda^3/gf) = -\theta \chi_u + C$ with $\theta = 5040/T$, where I is the line intensity integrated over the observed profile, λ is the transition wavelength, g and f are the statistical weight of the lower level and the oscillator strength, χ_u is the excitation energy of the upper level in eV, and T is the excitation temperature. The excitation temperature is empirically derived by fitting multiple Fe I lines spanning a range of upper-level energies. The fitted constant C is then used to derive column densities and production rates accounting for solar dilution, and the partition function, following the formalism of Manfroid et al. (2021). Consistent with their findings, we adopt $T(\text{Ni I}) = T(\text{Fe I}) + 180$ K. Atomic parameters for Fe and Ni transitions are taken from the NIST Atomic Spectra Database (Kramida et al. 2024).

The derived Fe and Ni production rates are $Q_{\text{Fe}} = (9.55 \pm 3.96) \times 10^{25}$ atoms s^{-1} , and $Q_{\text{Ni}} = (6.61 \pm 2.74) \times 10^{25}$ atoms s^{-1} . The logged ratio is $\log(Q_{\text{Ni}}/Q_{\text{Fe}}) = -0.16 \pm 0.03$, which is more Fe-rich than pre-perihelion ratios from Hutsemékers et al. (2025) ($\log(Q_{\text{Ni}}/Q_{\text{Fe}}) = 0.60 \pm 0.04$) though not as much so as the solar abundance of $\log(\text{Ni/Fe})_{\odot} = -1.25 \pm 0.04$ (Asplund et al. 2009).

Table 1. Best-fit values for the production rate power law fits in Figure 4. A is a constant and n is the power-law index.

Species	A	n	
			s^{-1}
CN	$(4.6 \pm 1.7) \times 10^{26}$	-3.72 ± 0.62	
C_2	$(2.8 \pm 0.7) \times 10^{26}$	-2.69 ± 0.47	
C_3	$(4.5 \pm 1.8) \times 10^{24}$	$+0.24 \pm 0.88$	

3.2. Radial Distributions

Our IFU data enable spectro-spatial analyses of the emission species in 3I/ATLAS. At $\Delta = 2.089$ au, the entire KCWI field of view corresponds to a projected physical size of $\sim 30\,000 \times 25\,000$ km. 3I/ATLAS filled the entire medium slicer in acquisition images. Figure 5 shows the KCWI 2D narrow-band images for spectral regions dominated by each observed feature: Ni, Fe, CN, C_3 , and C_2 . The CN emission is the most extensive.

We next fit the radial profiles of Ni, Fe, CN, C_3 , and C_2 with the same exponential decay model as Hoogendam et al. (2025a), which is defined as

$$A \times \exp\left[\frac{-x}{\tau}\right] + C, \quad (2)$$

where τ is the characteristic e -folding length scale of the radial profile and A and C are nuisance parameters. To account for differences in continuum level, we normalize the data to the maximum flux value. We use sigma-clipping with ten fit iterations to remove outliers.

The apparent spatial extent of an emission depends on where the emitting species is produced, either directly from nucleus-released volatiles or from a distributed grain source in the coma, and on how long the species survives before being destroyed by sunlight. CN is efficiently produced from a volatile parent and survives a long time as a radical, giving it a large daughter scale length and a bright profile that persists far down the tailward coma. For C_2 and C_3 there may be distributed sources (e.g., organic-rich grains) and multi-step chemistry. This tends to make their spatial profiles different from CN and often less extended in the outer coma. Thus, it is unsurprising that CN has a longer e -folding length scale than the other species observed in 3I/ATLAS.

Figure 6 shows our fits to the azimuthally averaged flux as a function of the physical radial distance for each emission feature; the best-fit parameters of the fits are given in Table 2. The CN flux is far more dispersed than

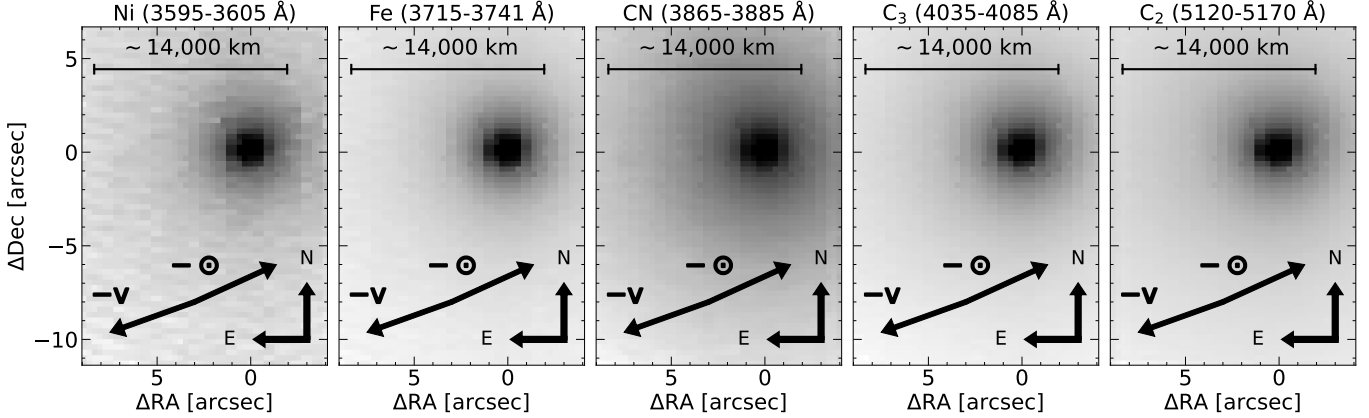


Figure 5. Comparison of narrow-band images from the KCWI data cube in the spectral regions corresponding to Ni, Fe, CN, C₃, and C₂. The maximum value of each panel is set individually.

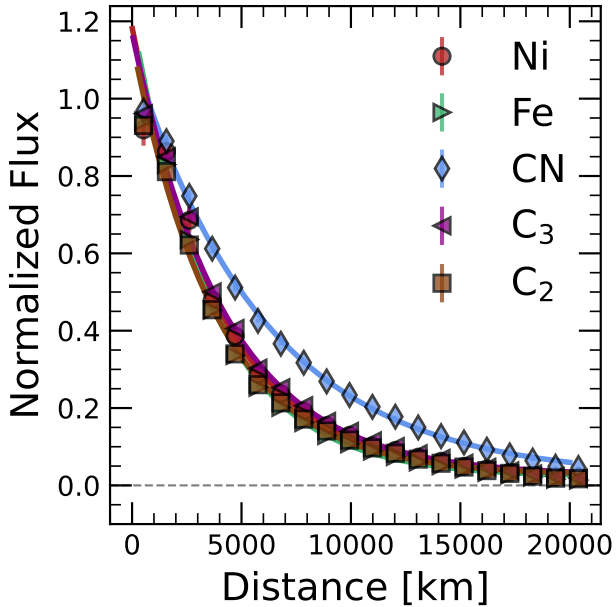


Figure 6. Measured radial profiles of Ni, Fe, CN, C₃ and C₂ in 3I/ATLAS measured using the images shown in Figure 5. The maximum unbinned flux values for each feature are normalized to 1 to correct for luminosity differences. Each point denotes radially binned data with a radius step size of 1046 km. Exponential fits are overplotted.

the other species, with a characteristic *e*-folding length-scale ~ 2000 km longer. This lengthscale increased by a factor of ~ 7 from the pre-perihelion measurement of 841.0 ± 15.4 km from Hoogendam et al. (2025a). In comparison, the Ni *e*-folding lengthscale increased by a factor of ~ 6.5 .

Speculatively, the increase in *e*-folding radius is not what is expected from heliocentric-distance scaling, indicating a possible change in the dominant source and/or kinematics of the radicals. Enhanced, post-perihelion

Table 2. Best fit values for the radial profiles in Figure 6.

Species	<i>A</i> [km]	τ [km]	<i>C</i> [km]
Ni	1.112 ± 0.009	3880.2 ± 39.3	0.110 ± 0.001
Fe	1.105 ± 0.009	3694.9 ± 36.3	0.092 ± 0.001
CN	0.748 ± 0.004	6053.1 ± 67.6	0.333 ± 0.002
C ₃	1.028 ± 0.008	4193.9 ± 44.9	0.128 ± 0.002
C ₂	0.994 ± 0.010	3833.4 ± 44.8	0.141 ± 0.001

activity, potentially driven by thermal lag, could produce more distributed sources through increased grain release or fragmentation. Additionally, seasonal effects associated with a potential high-obliquity rotation pole may modify the illumination of active regions. Together, stored heat near perihelion and changing seasonal illumination could enhance dust and gas release after perihelion, broadening the coma and increasing the role of distributed sources.

3.3. Symmetry and Jets

Following Hoogendam et al. (2025a), we construct an azimuthally symmetric model of the comet flux and subtract it from the white light images. The angular flux residual profile for each emission feature in 3I/ATLAS is shown in Figure 7. The model-subtracted image reveals excess flux in the anti-solar direction, consistent with a cometary tail. The residual is oversubtracted (by virtue of the spherical symmetry assumption) in the solar direction.

Interestingly, while the Ni, Fe, CN, and C₂ features are roughly aligned with the Sun (the anti-solar direction is 294.5° East of North), C₃ is misaligned with the

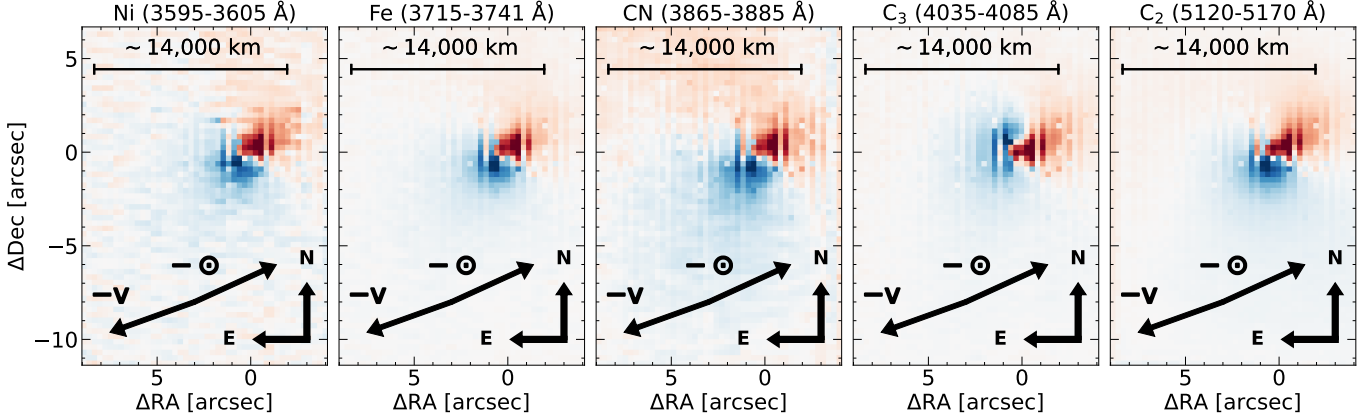


Figure 7. Comparison of the non-symmetric residuals from the KCWI data cube for Ni, Fe, CN, C₃ and C₂. Each image from Figure 5 is fit to determine the azimuthally averaged profile, which is then subtracted from the data. The resulting residuals show excess flux (red) and oversubtracted flux (blue). This excess flux corresponds to physical cometary emission (i.e., tails or jets), whereas the oversubtractions arise in the anti-tail direction.

anti-solar direction and the other emission features. One explanation could be that 3I/ATLAS, like Solar System comets, has an inhomogeneous composition, and the C₃ activity originates from a region enriched in longer-chain hydrocarbons in the surface that feeds a jet. For example, if the parent species of C₂ and C₃ are C₂H₂, C₂H₆, and C₃H₄ (e.g., [Helbert et al. 2005](#)), it may be the case that the C₃H₄ distribution is more localized to one region of the comet than those of C₂H₂ and C₂H₆, which could be more ubiquitous on the comet surface.

Alternatively, the reported sunward jet in pre-perihelion observations (e.g., [Serra-Ricart et al. 2026](#)) could potentially still be active and now pointing away from the Sun. If so, it may be possible that the pre-perihelion activity depleted that specific part of 3I/ATLAS of most of its volatiles, but heavier hydrocarbons remain and drive the C₃ activity in particular. This contrasts with other regions that are less sublimation-depleted, which would still emit bulk volatiles that are swept into an anti-solar tail. One challenge to this scenario is that the hydrocarbon parent species of C₂ do not seem to have the same dependence despite also originating from similarly heavy hydrocarbons.

Figure 7 also shows that the C₃ emission magnitude is less symmetrical around $\theta \approx 270$ degrees from North through East than the other features. This is likely due to additional flux contributions from C₂, which overlaps with the C₃ region (we do not see this effect for C₂, because our C₂ wavelength range excludes C₃ lines).

4. REMARKS ON THE COMPOSITION OF 3I/ATLAS

Pre-perihelion observations of Ni ([Rahatgaonkar et al. 2025](#); [Hoogendam et al. 2025a,b](#)) and Fe ([Hutsemékers et al. 2025](#)) emission reveal that 3I/ATLAS is an outlier

among Solar System comets in its Ni/Fe ratio, both compared to objects at distances of 2–3 au and the entire sample from [Manfroid et al. \(2021\)](#) regardless of r_h . Figure 8 shows the evolution of the logged Ni/Fe ratio for the [Manfroid et al. \(2021\)](#) sample of Solar System comets as a function of r_h . Unfortunately, no Solar System comet is as well-measured or as comprehensively observed as 3I/ATLAS.

3I/ATLAS shows strong, linear log(Ni/Fe) evolution as a function of r_h . We fit a line to the data and find a slope of 1.15 ± 0.05 (and an intercept of -1.89 ± 0.10). 3I/ATLAS has $\log(\text{Ni/Fe}) \approx 1.4$ at ~ 2.5 au, whereas the only two Solar System comets (both from the Oort cloud, [Oort 1950](#)) measured at comparable distance have values consistent with 0, suggesting either that 3I/ATLAS is extraordinarily enriched in Ni or the Solar System comparison sample does not capture the full diversity of cometary compositions and behaviors at that distance. 3I's evolution from an extreme outlier to outgassing Ni/Fe consistent with Solar System comets suggests that the latter is the most likely explanation.

With a perihelion distance of 1.36 au, 3I/ATLAS does not approach the Sun as closely as many of the comets from [Manfroid et al. \(2021\)](#). Few Solar System comets have more than one log(Ni/Fe) measurement, but those that do tend not to show the significant linear evolution seen in 3I/ATLAS. However, where changes have been observed at $r_h < 2$ au, they have been in the same direction: Ni/Fe generally increasing with r_h (see also [Rahatgaonkar et al. 2025](#); [Hutsemékers et al. 2025](#)).

5. CONCLUSIONS

We present the first post-perihelion IFU analysis of 3I/ATLAS. At the time of observation, 3I/ATLAS was at $r_h = 1.51$ au. We observe CN, Ni, and Fe activ-

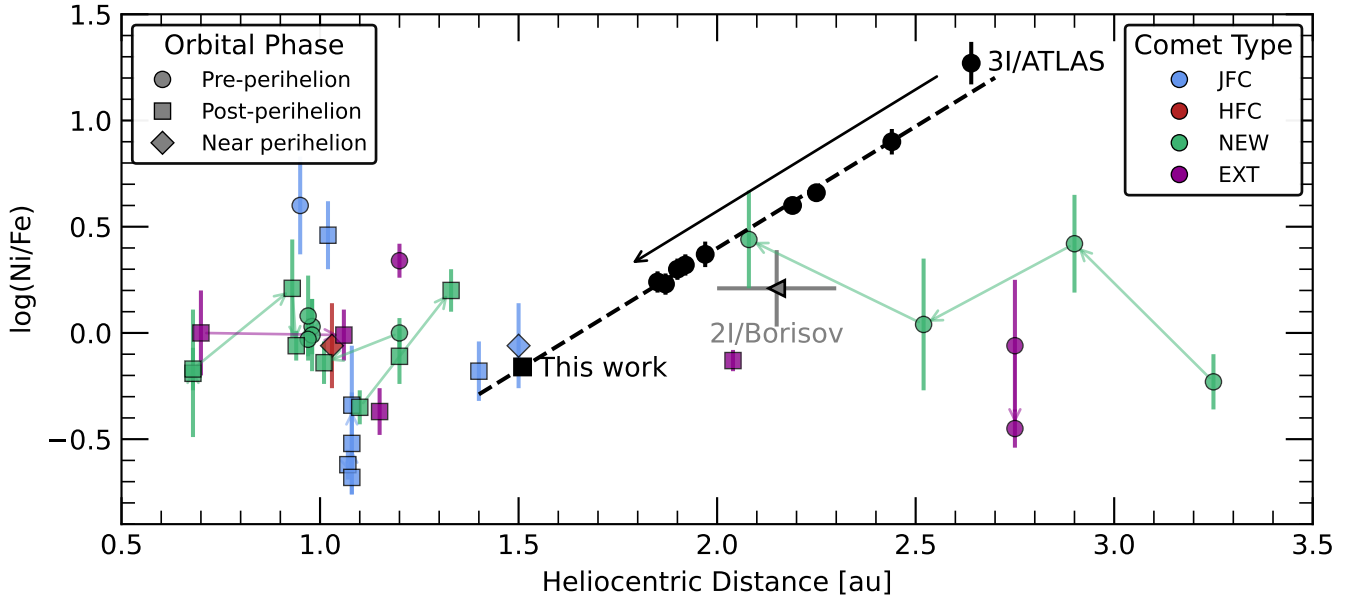


Figure 8. Ni/Fe ratio evolution for 3I/ATLAS (black circles; Hutsemékers et al. 2025 and this work, black square) compared to 2I/Borisov (Opitom et al. 2021) and Solar System comets (Manfroid et al. 2021). Comets connected with lines are repeat observations of the same comet, and the arrows denote the direction of movement. 3I/ATLAS initially had a higher Ni/Fe ratio than any other observed comet, but after its perihelion passage, it is similar to the Solar System comet 9P/Tempel 1. Comet classification follows Manfroid et al. (2021): JFCs are Jupiter-family comets, HFCs are Halley-family comets, NEW comets are dynamically new ($a < 10,000$ au), and EXT are directly from the Oort cloud ($a > 10,000$ au).

ity, which were also seen in pre-perihelion observations (e.g., Rahatgaonkar et al. 2025; Hoogendam et al. 2025a; Salazar Manzano et al. 2025; Hoogendam et al. 2025b; Hutsemékers et al. 2025). Additionally, we report C_2 , C_3 , and CH activity. The CN emission has a larger e -folding distance than the other species by a factor of ~ 1.5 , consistent with CN having a longer survival time as a radical.

We find evidence that the C_3 emission in particular may trace a jet emerging at a different angle than the other species. The jet may arise from either inhomogeneities in the surface composition of 3I/ATLAS or from continuation of the previously reported jets (e.g., Serra-Ricart et al. 2026). Further post-perihelion IFU data will improve the understanding of this feature.

3I/ATLAS has uniquely comprehensive pre- and post-perihelion observations that track the evolution of atomic Ni and Fe—something only one Solar System comet, C/2002 V1 (NEAT), has. Even if the driving mechanism for Ni emission in the solar system differs from that of interstellar comets, Ni and Fe measurements for interstellar comets offer a promising pathway to explore the primordial metallicity of other planetary systems. Continued post-perihelion observations will provide further insights into the post-perihelion evolution of the Ni/Fe ratio and how Fe and Ni emission may

eventually “turn off” with increasing heliocentric distance.

The Legacy Survey of Space and Time (Ivezic et al. 2019) will discover additional interstellar objects and, crucially, may detect many of them before their perihelion passage, enabling improved understanding of the solar radiation processing a perihelion passage induces on this type of object. Increasing the sample of interstellar and Solar System comets with detections of Ni and Fe will enable further population-level studies to understand the metal content of interstellar objects and the primordial planetary formation material in other solar systems.

ACKNOWLEDGMENTS

W.B.H. acknowledges support from the National Science Foundation Graduate Research Fellowship Program under Grant No. 2236415.

D.O.J. acknowledges support from NSF grants AST-2407632, AST-2429450, and AST-2510993, NASA grant 80NSSC24M0023, and HST/JWST grants HST-GO-17128.028 and JWST-GO-05324.031, awarded by the Space Telescope Science Institute (STScI), which is operated by the Association of Universities for Research in Astronomy, Inc., for NASA, under contract NAS5-26555.

The Shappee group at the University of Hawai‘i at Mānoa is supported by NSF (grant AST-2407205) and NASA (grants HST-GO-17087, 80NSSC24K0521, 80NSSC24K0490, 80NSSC23K1431).

K.J.M., J.J.W., and A.H. acknowledge support from the Simons Foundation through SFI-PD-Pivot Mentor-00009672. J.T.H. acknowledges support from NASA through the NASA Hubble Fellowship grant HST-HF2-51577.001-A, awarded by STScI. STScI is operated by the Association of Universities for Research in Astronomy, Incorporated, under NASA contract NAS5-26555.

C.A. and K.M. acknowledge support from NASA grants JWST-GO-02114, JWST-GO-02122, JWST-GO-03726, JWST-GO-04217, JWST-GO-04436, JWST-GO-04522, JWST-GO-05057, JWST-GO-05290, JWST-GO-06023, JWST-GO-06213, JWST-GO-06583, and JWST-GO-06677. Support for these programs was provided by NASA through a grant from the Space Telescope Science Institute, which is operated by the Association of Universities for Research in Astronomy, Inc., under NASA contract NAS5-03127.

Some of the data presented herein were obtained at Keck Observatory, which is a private 501(c)3 non-profit organization operated as a scientific partnership among the California Institute of Technology, the University of California, and the National Aeronautics and Space Administration. The Observatory was made possible by the generous financial support of the W. M. Keck Foundation.

This research has made use of the Keck Observatory Archive (KOA), which is operated by the W. M. Keck Observatory and the NASA Exoplanet Science Institute (NExScI), under contract with the National Aeronautics and Space Administration.

The authors wish to recognize and acknowledge the very significant cultural role and reverence that the summit of Maunakea has always had within the Native Hawaiian community. We are most fortunate to have the opportunity to conduct observations from this mountain.

This research made use of `PypeIt`⁹, a Python package for semi-automated reduction of astronomical data (Prochaska et al. 2020; Prochaska et al. 2020).

Facility: Keck:II (KCWI)

REFERENCES

A'Hearn, M. F., Millis, R. C., Schleicher, D. O., Osip, D. J., & Birch, P. V. 1995, *Icarus*, 118, 223, doi: [10.1006/icar.1995.1190](https://doi.org/10.1006/icar.1995.1190)

Arpigny, C., Bertaux, J. L., Bodechtel, J., et al. 1978, Workshop on cometary missions. ESOC Darmstadt, 17 - 19 April 1978. Chairmen's summaries and extended abstracts of invited contributions.

Asplund, M., Grevesse, N., Sauval, A. J., & Scott, P. 2009, *ARA&A*, 47, 481, doi: [10.1146/annurev.astro.46.060407.145222](https://doi.org/10.1146/annurev.astro.46.060407.145222)

Bannister, M. T., Opitom, C., Fitzsimmons, A., et al. 2020, arXiv e-prints, arXiv:2001.11605. <https://arxiv.org/abs/2001.11605>

Biver, N., Bockelée-Morvan, D., Crovisier, J., et al. 1999, *AJ*, 118, 1850, doi: [10.1086/301033](https://doi.org/10.1086/301033)

Bodewits, D., Bonev, B. P., Cordner, M. A., & Villanueva, G. L. 2024, in Comets III, ed. K. J. Meech, M. R. Combi, D. Bockelée-Morvan, S. N. Raymond, & M. E. Zolensky (University of Arizona Press), 407–432, doi: [10.2458/azu_uapress_9780816553631-ch013](https://doi.org/10.2458/azu_uapress_9780816553631-ch013)

Bolin, B., Wong, I., Lemaux, B., et al. 2025a, The Astronomer's Telegram, 17503, 1

Bolin, B., Wong, I., Abron, L.-M., et al. 2025b, The Astronomer's Telegram, 17561, 1

Borisov, G., Durig, D. T., Sato, H., et al. 2019, Central Bureau Electronic Telegrams, 4666, 1

Chandler, C. O., Bernardinelli, P. H., Jurić, M., et al. 2025, arXiv e-prints, arXiv:2507.13409, doi: [10.48550/arXiv.2507.13409](https://doi.org/10.48550/arXiv.2507.13409)

Cochran, A. L. 1985, *AJ*, 90, 2609, doi: [10.1086/113966](https://doi.org/10.1086/113966)

Cordiner, M. A., Roth, N. X., Kelley, M. S. P., et al. 2025, arXiv e-prints, arXiv:2508.18209, doi: [10.48550/arXiv.2508.18209](https://doi.org/10.48550/arXiv.2508.18209)

Cremonese, G., Fulle, M., Cambianica, P., et al. 2020, *ApJL*, 893, L12, doi: [10.3847/2041-8213/ab8455](https://doi.org/10.3847/2041-8213/ab8455)

de la Fuente Marcos, R., Alarcon, M. R., Licandro, J., et al. 2025, *A&A*, 700, L9, doi: [10.1051/0004-6361/202556439](https://doi.org/10.1051/0004-6361/202556439)

Denneau, L., Siverd, R., Tonry, J., et al. 2025, MPEC

Engelhardt, T., Jedicke, R., Vereš, P., et al. 2017, *AJ*, 153, 133, doi: [10.3847/1538-3881/aa5c8a](https://doi.org/10.3847/1538-3881/aa5c8a)

Fitzsimmons, A., Meech, K., Matrà, L., & Pfalzner, S. 2024, in Comets III, ed. K. J. Meech, M. R. Combi, D. Bockelée-Morvan, S. N. Raymond, & M. E. Zolensky, 731–766

Fitzsimmons, A., Hainaut, O., Meech, K. J., et al. 2019, *ApJL*, 885, L9, doi: [10.3847/2041-8213/ab49fc](https://doi.org/10.3847/2041-8213/ab49fc)

⁹ <https://pypeit.readthedocs.io/en/latest/>

Fray, N., Bénilan, Y., Cottin, H., Gazeau, M.-C., & Crovisier, J. 2005, *Planet. Space Sci.*, 53, 1243, doi: [10.1016/j.pss.2005.06.005](https://doi.org/10.1016/j.pss.2005.06.005)

Ganesh, S., Ahuja, G., Arvind, B., & Bhardwaj, A. 2025, The Astronomer's Telegram, 17502, 1

Gausset, L., Herzberg, G., Lagerqvist, A., & Rosen, B. 1965, *ApJ*, 142, 45, doi: [10.1086/148262](https://doi.org/10.1086/148262)

Guzik, P., & Drahus, M. 2021, *Nature*, 593, 375, doi: [10.1038/s41586-021-03485-4](https://doi.org/10.1038/s41586-021-03485-4)

Guzik, P., Drahus, M., Rusek, K., et al. 2020, *Nature Astronomy*, 4, 53, doi: [10.1038/s41550-019-0931-8](https://doi.org/10.1038/s41550-019-0931-8)

Haser, L. 1957, *Bulletin de la Societe Royale des Sciences de Liege*, 43, 740

Helbert, J., Rauer, H., Boice, D. C., & Huebner, W. F. 2005, *A&A*, 442, 1107, doi: [10.1051/0004-6361:20041571](https://doi.org/10.1051/0004-6361:20041571)

Hoogendam, W. B., Shappee, B. J., Wray, J. J., et al. 2025a, arXiv e-prints, arXiv:2510.11779, doi: [10.48550/arXiv.2510.11779](https://doi.org/10.48550/arXiv.2510.11779)

Hoogendam, W. B., Kuesters, D., Shappee, B. J., et al. 2025b, arXiv e-prints, arXiv:2512.09020. <https://arxiv.org/abs/2512.09020>

Huggins, W. 1881, *Proceedings of the Royal Society of London Series I*, 33, 1

Hui, M.-T., Ye, Q.-Z., Föhring, D., Hung, D., & Tholen, D. J. 2020, *AJ*, 160, 92, doi: [10.3847/1538-3881/ab9df8](https://doi.org/10.3847/1538-3881/ab9df8)

Hutsemékers, D., Manfroid, J., Jehin, E., et al. 2025, arXiv e-prints, arXiv:2509.26053, doi: [10.48550/arXiv.2509.26053](https://doi.org/10.48550/arXiv.2509.26053)

Ivezić, Ž., Kahn, S. M., Tyson, J. A., et al. 2019, *ApJ*, 873, 111, doi: [10.3847/1538-4357/ab042c](https://doi.org/10.3847/1538-4357/ab042c)

Jehin, E., Hmidaoui, S., Aravind, K., et al. 2025a, The Astronomer's Telegram, 17515, 1

—. 2025b, The Astronomer's Telegram, 17538, 1

Jehin, E., Gillon, M., Queloz, D., et al. 2011, *The Messenger*, 145

Jewitt, D., Hui, M.-T., Mutchler, M., Kim, Y., & Agarwal, J. 2025, *ApJL*, 990, L2, doi: [10.3847/2041-8213/adf8d8](https://doi.org/10.3847/2041-8213/adf8d8)

Jewitt, D., & Luu, J. 2019, *ApJL*, 886, L29, doi: [10.3847/2041-8213/ab530b](https://doi.org/10.3847/2041-8213/ab530b)

Jewitt, D., Luu, J., Rajagopal, J., et al. 2017, *ApJL*, 850, L36, doi: [10.3847/2041-8213/aa9b2f](https://doi.org/10.3847/2041-8213/aa9b2f)

Jewitt, D., & Seligman, D. Z. 2023, *ARA&A*, 61, 197, doi: [10.1146/annurev-astro-071221-054221](https://doi.org/10.1146/annurev-astro-071221-054221)

Kim, Y., Jewitt, D., Mutchler, M., et al. 2020, *ApJL*, 895, L34, doi: [10.3847/2041-8213/ab9228](https://doi.org/10.3847/2041-8213/ab9228)

Kramida, A., Ralchenko, Y., Reader, J., & NIST ASD Team. 2024, NIST Atomic Spectra Database, 5.12, <https://physics.nist.gov/asd>, doi: [10.18434/T4W30F](https://doi.org/10.18434/T4W30F)

Lantz, B., Aldering, G., Antilogus, P., et al. 2004, in Society of Photo-Optical Instrumentation Engineers (SPIE) Conference Series, Vol. 5249, Optical Design and Engineering, ed. L. Mazuray, P. J. Rogers, & R. Wartmann, 146–155, doi: [10.1117/12.512493](https://doi.org/10.1117/12.512493)

Lin, H. W., Lee, C.-H., Gerdes, D. W., et al. 2020, *ApJL*, 889, L30, doi: [10.3847/2041-8213/ab6bd9](https://doi.org/10.3847/2041-8213/ab6bd9)

Lisse, C. M., Bach, Y. P., Bryan, S., et al. 2025, arXiv e-prints, arXiv:2508.15469, doi: [10.48550/arXiv.2508.15469](https://doi.org/10.48550/arXiv.2508.15469)

Manfroid, J., Hutsemékers, D., & Jehin, E. 2021, *Nature*, 593, 372, doi: [10.1038/s41586-021-03435-0](https://doi.org/10.1038/s41586-021-03435-0)

McKay, A. J., Cochran, A. L., Dello Russo, N., & DiSanti, M. A. 2020, *ApJL*, 889, L10, doi: [10.3847/2041-8213/ab64ed](https://doi.org/10.3847/2041-8213/ab64ed)

Meech, K. J., Weryk, R., Micheli, M., et al. 2017, *Nature*, 552, 378, doi: [10.1038/nature25020](https://doi.org/10.1038/nature25020)

Meier, R., Wellnitz, D., Kim, S. J., & A'Hearn, M. F. 1998, *Icarus*, 136, 268, doi: [10.1006/icar.1998.6022](https://doi.org/10.1006/icar.1998.6022)

Micheli, M., Farnocchia, D., Meech, K. J., et al. 2018, *Nature*, 559, 223, doi: [10.1038/s41586-018-0254-4](https://doi.org/10.1038/s41586-018-0254-4)

Morrissey, P., Matuszewski, M., Martin, D. C., et al. 2018, *ApJ*, 864, 93, doi: [10.3847/1538-4357/aad597](https://doi.org/10.3847/1538-4357/aad597)

Neill, D., Matuszewski, M., Martin, C., Brodheim, M., & Rizzi, L. 2023, KCWI_DRP: Keck Cosmic Web Imager Data Reduction Pipeline in Python, Astrophysics Source Code Library, record ascl:2301.019. <http://ascl.net/2301.019>

Oort, J. H. 1950, *BAN*, 11, 91

Opitom, C., Fitzsimmons, A., Jehin, E., et al. 2019, *A&A*, 631, L8, doi: [10.1051/0004-6361/201936959](https://doi.org/10.1051/0004-6361/201936959)

Opitom, C., Jehin, E., Hutsemékers, D., et al. 2021, *A&A*, 650, L19, doi: [10.1051/0004-6361/202141245](https://doi.org/10.1051/0004-6361/202141245)

Opitom, C., Snodgrass, C., Jehin, E., et al. 2025, arXiv e-prints, arXiv:2507.05226, doi: [10.48550/arXiv.2507.05226](https://doi.org/10.48550/arXiv.2507.05226)

ʻOumuamua ISSI Team, Bannister, M. T., Bhandare, A., et al. 2019, *Nature Astronomy*, 3, 594, doi: [10.1038/s41550-019-0816-x](https://doi.org/10.1038/s41550-019-0816-x)

Preston, G. W. 1967, *ApJ*, 147, 718, doi: [10.1086/149049](https://doi.org/10.1086/149049)

Prochaska, J. X., Hennawi, J. F., Westfall, K. B., et al. 2020, *Journal of Open Source Software*, 5, 2308, doi: [10.21105/joss.02308](https://doi.org/10.21105/joss.02308)

Prochaska, J. X., Hennawi, J., Cooke, R., et al. 2020, pypeit/PypeIt: Release 1.0.0, v1.0.0, Zenodo, doi: [10.5281/zenodo.3743493](https://doi.org/10.5281/zenodo.3743493)

Puzia, T. H., Rahatgaonkar, R., Carvajal, J. P., Nayak, P. K., & Luco, B. 2025, arXiv e-prints, arXiv:2508.02777, doi: [10.48550/arXiv.2508.02777](https://doi.org/10.48550/arXiv.2508.02777)

Rahatgaonkar, R., Carvajal, J. P., Puzia, T. H., et al. 2025, arXiv e-prints, arXiv:2508.18382, doi: [10.48550/arXiv.2508.18382](https://doi.org/10.48550/arXiv.2508.18382)

Salazar Manzano, L. E., Lin, H. W., Taylor, A. G., et al. 2025, ApJL, 993, L23, doi: [10.3847/2041-8213/ae1232](https://doi.org/10.3847/2041-8213/ae1232)

Seligman, D. Z., Micheli, M., Farnocchia, D., et al. 2025, ApJL, 989, L36, doi: [10.3847/2041-8213/adf49a](https://doi.org/10.3847/2041-8213/adf49a)

Serra-Ricart, M., Licandro, J., & Alarcon, M. R. 2026, A&A, 705, L3, doi: [10.1051/0004-6361/202558072](https://doi.org/10.1051/0004-6361/202558072)

Swan, W. 1857, Transactions of the Royal Society of Edinburgh, 21, 411–429, doi: [10.1017/S0080456800032233](https://doi.org/10.1017/S0080456800032233)

Tonry, J., Denneau, L., Alarcon, M., et al. 2025, arXiv e-prints, arXiv:2509.05562, doi: [10.48550/arXiv.2509.05562](https://doi.org/10.48550/arXiv.2509.05562)

Tonry, J. L., Denneau, L., Heinze, A. N., et al. 2018, PASP, 130, 064505, doi: [10.1088/1538-3873/aabadf](https://doi.org/10.1088/1538-3873/aabadf)

Trilling, D. E., Mommert, M., Hora, J. L., et al. 2018, AJ, 156, 261

Tucker, M. A., Shappee, B. J., Huber, M. E., et al. 2022, PASP, 134, 124502, doi: [10.1088/1538-3873/aca719](https://doi.org/10.1088/1538-3873/aca719)

Xing, Z., Bodewits, D., Noonan, J., & Bannister, M. T. 2020, ApJL, 893, L48, doi: [10.3847/2041-8213/ab86be](https://doi.org/10.3847/2041-8213/ab86be)

Xing, Z., Oset, S., Noonan, J., & Bodewits, D. 2025, ApJL, 991, L50, doi: [10.3847/2041-8213/ae08ab](https://doi.org/10.3847/2041-8213/ae08ab)

Yang, B., Meech, K. J., Connelley, M., & Keane, J. V. 2025, arXiv e-prints, arXiv:2507.14916, <https://arxiv.org/abs/2507.14916>

Yang, B., Li, A., Cordiner, M. A., et al. 2021, Nature Astronomy, doi: [10.1038/s41550-021-01336-w](https://doi.org/10.1038/s41550-021-01336-w)

Ye, Q., Kelley, M. S. P., Bolin, B. T., et al. 2020, AJ, 159, 77, doi: [10.3847/1538-3881/ab659b](https://doi.org/10.3847/1538-3881/ab659b)

Ye, Q.-Z., Zhang, Q., Kelley, M. S. P., & Brown, P. G. 2017, ApJL, 851, L5, doi: [10.3847/2041-8213/aa9a34](https://doi.org/10.3847/2041-8213/aa9a34)